Evidence for non-*s*-wave symmetry of the π gap in MgB_2 from intermodulation distortion measurements

Y. D. Agassi,[1] D. E. Oates,[2] and B. H. Moeckly[3]
[1]*Naval Surface Warfare Center, Carderock Division, Bethesda, Maryland 20817-5700, USA*
[2]*MIT Lincoln Laboratory, Lexington, Massachusetts 02420-9108, USA*
[3]*STI Inc., Santa Barbara, California 92111-2356, USA*
(Received 8 May 2009; revised manuscript received 1 September 2009; published 24 November 2009)

We present low-temperature low-power intermodulation-distortion (IMD) measurements of high-quality MgB_2 thin films that are inconsistent with presumed *s*-wave symmetry of the order parameter. The measurements were carried out in a stripline resonator at approximately 2 GHz between 1.8 K and T_c. The IMD arises from the nonlinear Meissner effect in which the penetration depth is dependent on the RF magnetic field. Specifically, the observed IMD vs temperature T for $T \ll T_c/2$ varies as T^{-2}, while for an *s*-wave gap symmetry in the clean limit, the low-temperature IMD decreases exponentially with decreasing temperature. We calculate the IMD from first principles for different order-parameter symmetries using a Green's function approach and compare the results with the measured data. We propose that the observed upturn in the low-temperature IMD implies an admixture of an order parameter with nodal lines into the energy gaps of MgB_2. Most likely, this admixture is prominent for the π gap. Within the constraints of the hexagonal crystal symmetry of MgB_2, the best fit with our IMD measurements is obtained with a gap $\Delta(\phi,T)=\Delta_0(T)\sin(6\phi)$, where ϕ is the azimuthal angle in the $\widehat{ab}$ plane, and $\Delta_0(T)$ is the amplitude, weakly temperature dependent at low temperatures. This gap symmetry entails six nodal lines. We also present low-temperature penetration-depth measurements that are consistent with the proposed nodal gap symmetry. To relate our proposition with existing literature, we review other low-temperature probes of the order-parameter symmetry. The literature presents conflicting results, some of which are in direct support of the symmetry proposed here.

DOI: 10.1103/PhysRevB.80.174522 PACS number(s): 74.70.Ad, 74.20.Rp, 74.78.Bz

I. INTRODUCTION

Third-harmonic generation and intermodulation-distortion products (IMD) of a superconductor constitute the lowest-order nonlinear responses to an electromagnetic field. The IMD arises from the nonlinear Meissner effect (NLME) in which the penetration depth is dependent on the RF magnetic field. Third-order IMD is the mixing of two tones and is experimentally simpler to measure than harmonic generation. As demonstrated for YBCO at microwave frequencies, where $\hbar\omega \ll \Delta$, ω and Δ denote the circular frequency and superconductor gap, respectively, this response is practically frequency independent, a factor that simplifies the analysis considerably. The low-temperature IMD is sensitive to the existence of low-energy excitations in the superconductor, hence to the presence of nodal lines or planes in the energy gap, such as with the *d*-wave gap symmetry of YBCO. The relationship of gap symmetry to IMD and the NLME has been examined both theoretically[1–3] and experimentally.[4–7] With nodal lines in the gap, the IMD response diverges with decreasing temperatures, while in the absence of low-energy excitations, as for a gap with *s*-wave symmetry, the response decays exponentially. The divergence at low T and the high sensitivity of the measurement technique constitute the advantages of the IMD as a probe for nodal lines in the gap. This methodology has been successfully applied to YBCO, where the IMD power has been experimentally observed to follow the theoretically predicted characteristic T^{-2} divergence at low temperatures,[3,4,7–9] and leads to the conclusion that YBCO exhibits an energy gap with nodal lines.

Recently, penetration-depth measurements have provided evidence that YBCO possesses multiple-gap symmetries with in-plane $(s+d)$-wave symmetry.[10,11] These measurements are not in conflict with the YBCO IMD data, since at low temperatures the IMD divergence as T^{-2} dominates the exponentially small contribution of the *s*-wave gap component. The presence of nodes in the gap leads to low-temperature divergence even in cases of mixed symmetry containing a small *s*-wave component as discussed in Sec. III.

In this paper, we extend the methodology of IMD measurements to MgB_2. We find that the measured IMD in MgB_2 increases at low temperature as T^{-2}, resembling that in YBCO. This result implies that MgB_2 has at least some admixture of a nodal gap. We will show rigorously that a mixture of nodeless and nodal gaps still lead to the IMD divergence at low temperature. We conjecture that it is the π gap that is either nodal or a mixture of nodeless and nodal with the nodal component dominating.

The physical properties of MgB_2 have been studied extensively with a variety of probes such as specific heat, ^{11}B NMR experiments, and penetration-depth measurements complemented by first-principles calculations.[12–15] These studies led to the conclusion that MgB_2 entails two gaps, underpinned by four disconnected Fermi-surface sheets. The larger gap, denoted by σ, results from pairing mediated by electron-phonon interaction in the boron planes. It corresponds to two, nested, cylinder-shaped Fermi surfaces aligned along the $\hat{c}$ direction. The smaller gap, denoted by π, involves motion of the Mg and B atoms and corresponds to two-dimensional and three-dimensional, torus-shaped Fermi surfaces. The common assertion is that both gaps are *s* wave.[12] Typical values reported are 6.8 meV for the σ and 1.8 meV for the π.[14]

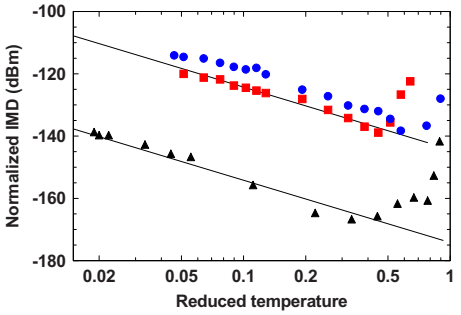

FIG. 1. (Color online) Comparison of IMD vs reduced temperature for representative MgB_2 samples and a typical YBCO sample (Ref. 4) at a circulating power of +5 dB m. ▲, YBCO, ● and ■, MgB_2 on sapphire articulating power of −5 dB m. The MgB_2 samples show higher IMD, but show the increase at low temperatures that is similar to that of YBCO. The low-temperature increase in the latter results from the *d*-wave symmetry of the energy gap.

Since MgB_2 has a single critical temperature, the gaps corresponding to the π and σ bands cannot be completely independent; there must be some off-diagonal terms that mix in the two gaps.[16,17] However, this mixing is expected to be small due to the rather different symmetries of the underlying bands.[18] Therefore MgB_2 can be approximately described in terms of two, effectively uncoupled gaps, i.e., the σ and π gaps. This point is discussed in more detail in Sec. III.

The characteristic low-temperature variation in the IMD in the clean limit for an *s*-wave gap symmetry is an exponential falloff [see Eq. (3.16)]

$$P_{\mathrm{IMD}}(T) \propto T^{-5} e^{-(2\Delta_0/k_B T)}, \tag{1.1}$$

where k_B is Boltzmann's constant. Our IMD-power measurements, Fig. 1, follow a qualitatively different low-temperature variation, even after accounting for sample variability across the several measured samples. The low-temperature IMD variation in Fig. 1 is in fact similar to that of high-quality YBCO films, also shown in Fig. 1,[4] where

$$P_{\mathrm{IMD}}(T) \propto T^{-2}. \tag{1.2}$$

Hence, unless our MgB_2 IMD data reflect some extrinsic factors, we are led to the conclusion that at least one of the gaps entails nodal lines or planes or both. The important issue regarding the effect of possible extrinsic factors is elaborated in Sec. VI, with the conclusion that most likely the data in Fig. 1 reflect the film's intrinsic response.

In the clean limit, the crystal-symmetry group imposes constraints on the allowable gap symmetries.[19] For the hexagonal crystal symmetry of MgB_2, out the four possible positive-parity gap symmetries, the best fit to our low-temperature IMD measurements is obtained with the gap function

$$\Delta(\phi, T) = \Delta_0(T)\sin(6\phi), \tag{1.3}$$

where ϕ is the azimuthal angle with respect to the $\hat{k}_x$ axis in the basal $\widehat{ab}$ plane. Details are given in Sec. III. To further test the proposed symmetry of Eq. (1.3), we compare its implication for our low-temperature penetration depth data and find good agreement.

Our findings naturally raise the question of consistency with existing literature on the MgB_2 gap symmetry. The literature reviewed in Sec. VII reveals conflicting data from different groups where several of the experiments support the notion of a nodal gap.

The paper is organized as follows. In Sec. II we describe the experimental approach, while Secs. III and IV describe the theoretical analysis of the low-temperature variations in the IMD power and penetration depth in the clean limit. Section V is a comparison of theory to our data. In Sec. VI we discuss the possibility that our data are dominated by extrinsic effects whereas in Sec. VII we review the literature pertaining to the gap symmetry. Section VIII is devoted to a summary of our results and suggestions for additional experiments to test the proposed gap, Eq. (1.3).

II. EXPERIMENT

The IMD was measured by the stripline-resonator technique, described below,[4,5] employing thin films of MgB_2 that were deposited by the reactive-evaporation method,[20,21] in which boron is deposited in vacuum onto a substrate that rapidly rotates through a region of high-pressure magnesium vapor where the MgB_2 film is formed. This method yields very clean, stable, large-area, double-sided MgB_2 films on a multitude of substrate materials. The films were deposited onto 5-cm-diameter sapphire and lanthanum aluminate (LAO) substrates and have $T_c = 39$ K and low resistivity. The film thickness in these experiments was either 150 or 500 nm. More detail about the films is given in Ref. 22.

The films were patterned using standard photolithography and ion milling. After patterning, the wafers were diced, and the etched striplines were assembled with ground planes from the same wafer to form stripline resonators. The properties of the patterned line dominate the performance of the resonator because the current density is approximately a factor 100 higher in the line than in the ground plane. The stripline center-conductor width is 150 μm. The quality factor Q and resonant frequency f_0 of the resonators were measured as a function of the microwave power at temperatures between 1.8 K and T_c. The measurements were carried out at the fundamental frequency of 2.3 GHz for films on the sapphire substrates, and at 1.5 GHz for films on the LAO substrate. The third-order IMD was measured in the usual way, in which two closely spaced tones of equal power at frequencies f_1 and f_2 are combined and applied to the resonator. The frequencies are centered about the resonant frequency with a tone separation of approximately 1/32 of the low-power 3 dB bandwidth. The frequencies of the tones were adjusted at each power level and temperature to maintain the same relationship to the bandwidth and resonant frequency. The power P_{IMD} of the third-order mixing products at frequencies $2f_1 - f_2$ and $2f_2 - f_1$ is then measured in a spectrum analyzer as a function of the input power to the resonator.

For the data analysis, the measured P_{IMD} is converted to a normalized IMD power P_{NORM}, which removes the dependence of the IMD on the unloaded Q value of the resonator and insertion loss[5]

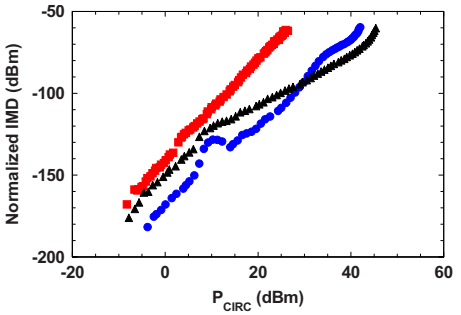

FIG. 2. (Color online) Typical measurements of normalized IMD power IMD (dB m)P_{NORM} vs P_{CIRC} at three selected temperatures. ■; $T=35$ K; ▲, $T=1.8$ K, and ●, $T=15$ K. The MgB_2 film is deposited on LAO. More temperatures were measured but are not shown for reasons of clarity. As discussed in the text, the slopes depart from the expected slope of three.

$$P_{\mathrm{NORM}} = \frac{P_{\mathrm{IMD}}}{r_v(1-r_v)Q_c}. \tag{2.1}$$

In Eq. (2.1) r_v denotes the voltage insertion ratio, which is related to the insertion loss IL in dB by

$$r_v = 10^{-IL/20} \tag{2.2}$$

and Q_c is the unloaded Q of the resonator. The input power P is converted to circulating power P_{CIRC} associated with the standing wave in the resonator at resonance according to the expression

$$P_{\mathrm{CIRC}} = \frac{4Q_l(1-r_v)r_vP}{\pi}, \tag{2.3}$$

The data are then plotted as normalized IMD power P_{NORM} vs P_{CIRC}. Figure 2 shows data measured at the indicated temperatures for a representative sample on a LAO substrate. Note that the IMD generally increases with a slope between 2 and 3 in the double logarithmic plot, and the slopes vary with temperature and input power. The question of slope values has been discussed in the literature and is beyond the scope of this paper.[7]

The focus of this work is the IMD vs temperature at a fixed, low circulating power. The data, however, are of necessity measured at fixed values of temperature with varying input power. In order to extract the IMD vs T curve from the measured data, we select a value of circulating power and make a polynomial fit to the data in the vicinity of that circulating power. The values of P_{NORM} are then extracted from these fits.

Figure 3 is a plot of IMD (P_{NORM}) vs temperature at $P_{\mathrm{CIRC}}=-5$ dB m circulating power, a fairly low value, for five different samples on sapphire and LAO substrates. All samples except one show an upturn at low temperatures, which is the focus of the rest of this paper. As was found in YBCO,[7] the IMD magnitude varies from sample to sample. Unlike the IMD measurements in YBCO,[4,7] the measured MgB_2 data show structure, which is not well understood and is discussed in later sections of this paper.

In addition to the IMD, the stripline resonator is used to measure small variations in the penetration depth λ_0 as a

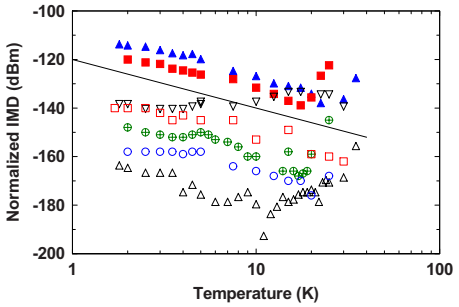

FIG. 3. (Color online) Normalized IMD vs temperature for representative samples from different fabrication runs all measured at −5 dB m circulating power. Samples were deposited under the same conditions. The open symbols are for samples 500 nm thick, and the closed symbols are for samples 150 nm thick. The substrates are sapphire except for the △ symbols which depict a film on LAO. All samples except the one depicted with ▽ show the $1/T^2$ increase at low temperature. The solid line is a $1/T^2$ dependence to guide the eyes. The sample that does not show a low-temperature increase has the highest IMD of the thicker samples, indicating that it is dominated by extrinsic IMD sources which mask the intrinsic $1/T^2$ dependence of the other samples. The 150-nm-thick samples have higher IMD at the same circulating power since the current density in them is higher.

function of temperature by measuring the change in resonance frequency $f(T)$. This method, however, does not yield the absolute value of λ_0. The change in the resonance frequency Δf can be related to the change in penetration depth by[23]

$$-\frac{2\Delta f}{f} = \frac{\Delta L}{L} = \frac{2\lambda_0\Delta\lambda\int J^2(x,y,\lambda)dA}{\int \mu_0 H^2(x,y)dA} \tag{2.4}$$

where L is the inductance per unit length of the stripline, J is the current density in the stripline, and H is the RF magnetic field in the dielectric. Equation (2.4) is based on the assumption that the change in reactance is due entirely to the change in kinetic inductance arising from the change in λ_0. This is a standard assumption. Since the current density in a stripline is dependent on λ_0, the integral in Eq. (2.4) must be evaluated numerically[23] and an iterative method used to determine $\Delta\lambda$.

III. THEORY OF IMD

We follow the approach developed for and applied to the IMD power in YBCO in the clean limit.[3] In this approach the focus is on the constitutive relation that relates the pair current to the vector potential in momentum space, which is of the form

$$\vec{j}_S(\vec{q}) = -\frac{c}{4\pi}K(\vec{q})\vec{A}(\vec{q}) = -\frac{c}{4\pi}\left\{\frac{1}{\lambda_0^2} + K_{NL}(|\vec{A}(\vec{q})|^2)\right\}\vec{A}(\vec{q}). \tag{3.1}$$

In Eq. (3.1) the pair-current density is denoted by $\vec{j}_S(\vec{q})$, $\vec{A}(\vec{q})$ denotes the vector potential in the static limit, $K(\vec{q})$ and

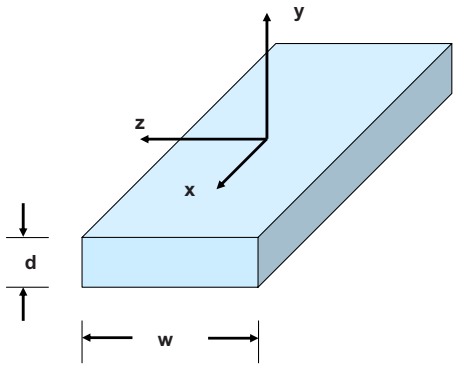

FIG. 4. (Color online) Coordinate system for the calculations.

$K_{NL}(|\vec{A}(\vec{q})|^2)$ denote the total and nonlinear kernels of the constitutive kernel, respectively, and c is the speed of light. The cgs unit system is employed throughout this work. The nonlinearity of the kernel K_{NL} is reflected in its dependence on the vector potential and is embodied in its Taylor series expansion

$$K_{NL}(|\vec{A}(q_z)|^2) = K^{(2)}(q_z)|\vec{A}(q_z)|^2 + K^{(4)}(q_z)|\vec{A}(q_z)|^4 + \cdots . \tag{3.2}$$

Figure 4 shows the chosen coordinate system. For the thin films employed in our experiments, a one-dimensional geometry is appropriate and the Miessner effect occurs at the film edges. Thus, the current flows along the $\hat{x}$ direction, is assumed uniform along the (thickness) $\hat{y}$ direction, but varies along the $\hat{z}$ direction, i.e.,

$$\vec{j}_S(\vec{x}) = \hat{x}j_{Sx}(z), \quad \vec{A}(\vec{x}) = \hat{x}A_x(z), \quad \vec{q} = (0,0,q_z),$$

$$\begin{pmatrix} \vec{A}(\vec{q}) \\ \vec{j}(\vec{q}) \end{pmatrix} = \int d\vec{x} e^{-i\vec{q}\cdot\vec{x}} \begin{pmatrix} \vec{A}(\vec{x}) \\ \vec{j}(\vec{x}) \end{pmatrix} = (2\pi)^2 \delta(q_x)\delta(q_y) \left(\begin{pmatrix} A_x(q_z) \\ j_x(q_z) \end{pmatrix}, 0, 0 \right),$$

$$\begin{pmatrix} A_x(q_z) \\ j_x(q_z) \end{pmatrix} = \int dz e^{-iq_z z} \begin{pmatrix} A_x(z) \\ j_x(z) \end{pmatrix}. \tag{3.3}$$

The IMD power is associated with the lowest-order term in expansion (3.2). This term and the higher-order terms have been calculated in the Green's function approach for the clean limit.[3] In particular, the explicit expression in the long-wavelength limit for a single gap is

$$K^{(2)}(q_z = 0)|\vec{A}(q_z = 0)|^2 \vec{A}(q_z = 0) = \frac{q_S^4 \alpha}{4\pi^4 \hbar^6 m \beta c^4 \lambda_0^2} \sum_{n=-\infty}^{\infty} \int d\vec{k}\vec{k}[\vec{A}(q_z = 0)\cdot\hat{k}]^3 \times \left(\frac{\partial \xi_{\vec{k}}}{\partial k_x} \right)^3 \{[\hat{G}_0(\vec{k}, \omega_n)]^4\}_{(1,1)},$$

$$\beta = \frac{1}{k_B T}, \quad \omega_n = \frac{(2n+1)\pi}{\beta\hbar}. \tag{3.4}$$

In Eq. (3.4) q_S is the single-carrier charge (positive or negative), α is a dimensionless number on the order of unity, $\hat{k}$ denotes a unit vector associated with the momentum vector $\vec{k}$, $\xi_{\vec{k}} = \varepsilon_{\vec{k}} - \mu$ is the band energy $\varepsilon_{\vec{k}}$ relative to the chemical potential μ, $\hat{G}_0$ denotes the homogeneous-superconductor Green's function matrix, and ω_n are the Matsubara frequencies. In case of more than one band (gap) and a single T_c, there must be matrix elements that mix the gaps.[16,17] The admixed gaps have to be calculated self-consistently.[11,16,17] For MgB_2 with a single T_c, the matrix elements that mix the two gaps are very small,[18] hence admixtures are expected to be weak. The corresponding two-band Green's function matrix is of dimensionality 4×4 with a 2×2 block corresponding to each band and small, off-diagonal matrix elements that mix the diagonal blocks.[24–26] Therefore, for MgB_2 the nonlinear kernel in Eq. (3.1) can be expanded as

$$K^{(2)}(q_z = 0) = K_\sigma^{(2)} + K_\pi^{(2)} + K_{\pi\sigma}^{(2)}, \tag{3.5}$$

where the kernels $K_\sigma^{(2)}$ and $K_\pi^{(2)}$ involve solely the diagonal blocks of the σ and π bands, respectively, while the $K_{\pi\sigma}^{(2)}$ kernel involves matrix elements that couple the (1,2) and (3,4) blocks. Provided these coupling matrix elements are sufficiently small in comparison to the diagonal terms, the $K_{\pi\sigma}^{(2)}$ kernel can be neglected in comparison to the $K_\sigma^{(2)}$ and $K_\pi^{(2)}$ kernels. This approximation corresponds to the uncoupled-gap model adopted in this work, where the σ and π gaps are treated individually, as in Eq. (3.4). Hence,

$$K_\sigma^{(2)} \propto \sum_{n=-\infty}^{\infty} \int d\vec{k}\vec{k}[\vec{A}(q_z = 0)\cdot\hat{k}]^3 \left(\frac{\partial \xi_{\vec{k}}(\sigma)}{\partial k_x} \right)^3 \{[\hat{G}_0(\vec{k}, \omega_n)]^4\}_{(1,1)},$$

$$K_\pi^{(2)} \propto \sum_{n=-\infty}^{\infty} \int d\vec{k}\vec{k}[\vec{A}(q_z = 0)\cdot\hat{k}]^3 \times \left[\frac{\partial \xi_{\vec{k}}(\pi)}{\partial k_x} \right]^3 \{[\hat{G}_0(\vec{k}, \omega_n)]^4\}_{(3,3)}. \tag{3.6}$$

The IMD power calculation for a single-band (gap) superconductor, Eq. (3.4), starts with the exact summation of the Matsubara-frequency dependence

$$\sum_{n=-\infty}^{\infty} \{[\hat{G}_0(\vec{k}, \omega_n)]^4\}_{(1,1)} = -\left(\frac{\beta^4\hbar^4}{48} \right)[-2 + \cosh(\beta\sqrt{\Delta^2 + \xi^2})]\mathrm{sech}^4\left(\frac{\beta}{2}\sqrt{\Delta^2 + \xi^2} \right). \tag{3.7}$$

In Eq. (3.7) the symbol Δ denotes the gap where its temperature and $\vec{k}$ dependencies have been suppressed to simplify notation. Note that by inserting the explicit expressions for $\hat{G}_0$ into the left-hand side of Eq. (3.7) it follows (not shown here) that for low temperatures, i.e., when $\beta\Delta \gg 1$, the low-n terms are positive while the $n \gg 1$ terms are negative. These two groups of terms almost cancel, where the latter is

slightly larger than the former. This near cancellation poses a challenge for a numerical summation of Eq. (3.7).

Inserting Eq. (3.7) into Eq. (3.6) and taking the long-wavelength limit we find for the nonlinear kernel in the one-dimensional geometry defined in Fig. 4 the general expression

$$K^{(2)}(q_z=0;\pi) = -\frac{1}{2^6 3\pi^4}\frac{q_S^4\alpha\beta^3}{(mc^2)(\hbar c)^2\lambda_0^2}\int dk_x\int dk_y\int dk_z k_x\left(\frac{\partial\xi_\pi}{\partial k_x}\right)^3 \times[-2+\cosh(\beta\sqrt{\Delta_\pi^2+\xi_\pi^2})]\mathrm{sech}^4\left(\frac{\beta}{2}\sqrt{\Delta_\pi^2+\xi_\pi^2}\right). \tag{3.8}$$

This applies for the π gap as the integration is three dimensional. The $\vec{k}$ dependence of ξ and Δ have been suppressed to simplify notation. For the particular case of $\hat{c}$-axis-aligned cylindrical Fermi surfaces and a gap with s-wave symmetry (the σ band), Eq. (3.8) takes the form

$$K^{(2)}(q_z=0;\sigma) = -\frac{1}{2^8\pi^3}\frac{q_S^4\alpha\beta^3}{(mc^2)(\hbar c)^2\lambda_0^2}\int K^2dK\int dk_z\left(\frac{\partial\xi_\sigma}{\partial K}\right)^3 \times[-2+\cosh(\beta\sqrt{\Delta_\sigma^2+\xi_\sigma^2})]\mathrm{sech}^4\left(\frac{\beta}{2}\sqrt{\Delta_\sigma^2+\xi_\sigma^2}\right), \tag{3.9}$$

where K and k_z denote the radial and z components in the cylindrical coordinate system.

In terms of the nonlinear kernels of Eq. (3.6) the single-band expression for the IMD power is[3]

$$P_{\mathrm{IMD}}(T)\propto[K^{(2)}(q_z=0)]^2. \tag{3.10}$$

Equation (3.10) is readily generalized for the case of a superconductor with two coupled bands.

$$P_{\mathrm{IMD}}\propto[K^{(2)}(q_z=0)]^2=[K_\sigma^{(2)}+K_\pi^{(2)}+K_{\pi\sigma}^{(2)}]^2 \approx[K_\sigma^{(2)}]^2+[K_\pi^{(2)}]^2. \tag{3.11}$$

Equation (3.11) entails two approximations. The first is the neglect of the kernel $K_{\pi\sigma}^{(2)}$, provided the off-diagonal coupling terms in the 4×4 Green's function are sufficiently small. As discussed above, this approximation is well justified.[18] The second, implicit approximation in Eq. (3.11) is the neglect of interference term between the σ and π kernels at the low-temperature limit which is at the focus of this work. This approximation conforms to our presumption that the σ gap and π gap are predominantly s wave and non-s wave (nodal gap), respectively. This point is further discussed in Sec. VII. Under these simplifying approximations, Eq. (3.11) implies that the analysis can proceed on a single-gap configuration, to which we turn now.

To evaluate the low-temperature behavior of $P_{\mathrm{IMD}}(T)$ when $\beta\Delta\gg1$, we consider first the Green's function factor, Eq. (3.7). In the low-temperature limit, this is the fastest-varying factor in the integrand, and it can be simplified to

$$\lim_{\beta\Delta\gg1}[-2+\cosh(\beta\sqrt{\Delta^2+\xi^2})]\mathrm{sech}^4\left(\frac{\beta}{2}\sqrt{\Delta^2+\xi^2}\right)=8e^{-\beta\sqrt{\Delta^2+\xi^2}}. \tag{3.12}$$

Furthermore, transforming the integration in Eq. (3.8) to cylindrical coordinates and invoking a change in variables $K\to\xi$ yields

$$K_\pi^{(2)}(q_z=0)=C_1\beta^3\int_{-\infty}^{\infty}d\xi\int_0^{2\pi}d\varphi\int_{-k_c}^{k_c}dk_z \times\left[K^2\left(\frac{\partial K}{\partial\xi}\right)\left(\frac{\partial\xi}{\partial k_x}\right)^3\cos(\varphi)\right]e^{-\beta\sqrt{\xi^2(\vec{k})+\Delta(\vec{k},T)^2}}. \tag{3.13}$$

In Eq. (3.13), all temperature-independent factors and the weakly varying $\lambda_0(T)$ factor in Eq. (3.8) are lumped into the constant C_1. Moreover, since the exponential is the fastest-varying factor in Eq. (3.13) it is justified to pull out all factors in the curly brackets from under the integral sign and replace them by a suitable average value, whose details, including the band structure $\xi(\vec{k})$ specifics, are unimportant. This step leaves only the exponential factor in the integrand of Eq. (3.13). The remaining integrations must be carried out exactly. The ξ integration gives the exact result[27]

$$\int_{-\infty}^{\infty}d\xi e^{-\beta\sqrt{\Delta^2+\xi^2}}=2\sqrt{\Delta^2}K_1(\beta\sqrt{\Delta^2})\approx\sqrt{\frac{2\pi\sqrt{\Delta^2}}{\beta}}e^{-\beta\sqrt{\Delta^2}}. \tag{3.14}$$

In Eq. (3.14) the symbol $K_1(z)$ denotes the modified Bessel function that is approximated by its asymptotic limit.[28] Pulling the curly bracket factors from under the integration in Eq. (3.13) and carrying out the associated ξ integration yields for the low-temperature limit of the nonlinear kernel

$$K_\pi^{(2)}(q_z=0;T)\approx C_2\beta^{5/2}\int_0^{2\pi}d\varphi\int_{-k_c}^{k_c}dk_z[\Delta(\varphi,k_z;T)^2]^{1/4}e^{-\beta\sqrt{\Delta(\varphi,k_z;T)^2}}, \tag{3.15}$$

where all the above-mentioned slowly varying factors in temperature are lumped into the constant C_2 and the remaining temperature and momentum dependencies have been made explicit. For an s-wave gap symmetry, $\Delta(\varphi,k_z;T)=\Delta_0(T)$, the φ and k_Z integrations in Eq. (3.15) collapse into a constant factor.

The structure of expression (3.15) shows that the low-temperature variation in the kernel strongly depends on the φ and k_z dependencies of the gap. These, in turn, are constrained by the hexagonal crystal-symmetry group of MgB_2.[19] Limiting ourselves to the positive-parity, one-dimensional representations for the hexagonal crystal-symmetry group, there are only four possibilities. These are listed in Table I with corresponding gap functions that are parameterized such that the amplitudes, $\Delta_0(T)$, are positive and have dimensionality of energy. Note that the Γ_1^+ gap with

TABLE I. Even-parity one-dimensional gap structure for the hexagonal lattice symmetry.

Irreducible representation	Basis function	Gap parametrization	Nodal structure
Γ_1^+	$1, k_x^2+k_y^2$	$\Delta(T)=\Delta_0(T)$	No nodal lines, planes
Γ_1^+	k_z^2	$\Delta(k_z;T)=\Delta_0(T)k_z^2/k_c^2$	Nodal plane
Γ_2^+	$-\frac{1}{2}\sin(6\phi)$	$\Delta(\varphi,T)=\Delta_0(T)\sin(6\varphi)$	Six nodal lines
Γ_3^+	$k_z\cos(3\phi)$	$\Delta(\varphi,k_z;T)=\Delta_0(T)\frac{k_z}{k_c}\cos(3\varphi)$	Nodal plane and three nodal lines
Γ_4^+	$-k_z\sin(3\phi)$	$\Delta(\varphi,k_z;T)=\Delta_0(T)\frac{k_z}{k_c}\sin(3\varphi)$	Nodal plane and three nodal lines

symmetry $k_x^2+k_y^2=K^2$ is taken as a constant since for both π and σ bands the Fermi surface is characterized by an approximately constant K value.[29,30]

With the gap parametrizations of Table I, the corresponding low-temperature IMD temperature variations are derived from Eq. (3.15). Table II summarizes the ensuing temperature dependencies for all possible gap parametrizations of Table I. Details are differed to the Appendix.

As an illustration of P_{IMD}, consider the simple case of an s-wave symmetry, i.e., the Γ_1^+ gap listed in the first line in Table I. In this case Eq. (3.15) yields

$$P_{\mathrm{IMD}}(T) \propto \beta^5 \Delta_0(T) e^{-2\beta\Delta_0(T)}. \tag{3.16}$$

As Eq. (3.16) indicates, for an s-wave gap the low-temperature variation in $P_{\mathrm{IMD}}(T)$ is exponentially decreasing with temperature, Eq. (1.1), reflecting the freeze-out of all thermal excitations in this temperature domain.

IV. THEORY OF THE PENETRATION DEPTH

In the clean low-power limit, the expression of the penetration depth in terms of the Green's function is[31]

$$\frac{1}{\lambda_0^2(T)} = \frac{q_S^2}{\pi^2 mc^2\hbar^2\beta}\sum_{n=-\infty}^{\infty}\int d\vec{k}\left[\frac{\partial\xi(\vec{k})}{\partial k_x}\right]\{[\hat{G}_0(\vec{k},\omega_n)]^2\}_{(1,1)} + \frac{4\pi q_S^2}{mc^2}n_{TOTAL}. \tag{4.1}$$

The chosen coordinate system is defined in Fig. 4, and n_{TOTAL} denotes the total single-carrier density.

To establish the low-temperature limit of $\lambda_0(T)$ we follow the method detailed in Sec. III. Consequently, we first perform the exact summation over the Matsubara frequencies. This yields

$$\sum_{n=-\infty}^{\infty}\{[\hat{G}_0(\vec{k},\omega_n)]^2\}_{(1,1)} = -\left(\frac{\beta^2\hbar^2}{4}\right)\mathrm{sech}^2\left(\frac{\beta}{2}\sqrt{\Delta^2+\xi^2}\right). \tag{4.2}$$

Inserting Eq. (4.2) into Eq. (4.1) and introducing the relation between the paired single-carrier density $n_s(T)$ and the penetration depth from the phenomenological London's theory[32]

$$\frac{1}{\lambda_0^2(T)} = \frac{4\pi n_s(T) q_s^2}{mc^2} \tag{4.3}$$

yields the general, well-convergent expression

$$\frac{n_s(T)}{n_{TOTAL}} = \left(\frac{\lambda_0(T=0)}{\lambda_0(T)}\right)^2 = 1 - \frac{\beta}{16\pi^3 n_{TOTAL}} \times \int d\vec{k}k_x\frac{\partial\xi(\vec{k})}{\partial k_x}\mathrm{sech}^2\left(\frac{\beta}{2}\sqrt{\Delta(\vec{k},T)^2+\xi(\vec{k})^2}\right). \tag{4.4}$$

To check expression (4.4) consider the textbook case of an s-wave gap where $\Delta(\vec{k},T)=\Delta_0(T)$, and a parabolic band structure $\xi_{\vec{k}}=\frac{\hbar^2k^2}{2m}-\mu$. In this case it is convenient to use in Eq. (4.4) the polar coordinate system. The angular integrations then yield

TABLE II. Low-temperature variation of the π kernel, Eq. (3.15).

Irreducible representation	Gap parametrization	$K^{(2)}(q_z=0;\pi;T)/C_2$ [Eq. (3.15)] Low-T variation for $\beta\Delta_0(T)\gg 1$
Γ_1^+	$\Delta(T)=\Delta_0(T)$	$k_c\beta^{5/2}\sqrt{\Delta_0(T)}e^{-\beta\Delta_0(T)}$
Γ_1^+	$\Delta(k_z;T)=\Delta_0(T)k_z^2/k_c^2$	$k_c\beta^{3/2}/\sqrt{\Delta_0(T)}$
Γ_2^+	$\Delta(\varphi,T)=\Delta_0(T)\sin(6\varphi)$	$\frac{k_c\beta}{\Delta_0(T)}\{2+\frac{15}{4[\beta\Delta_0(T)]^2}+\cdots\}$
Γ_3^+	$\Delta(\varphi,k_z;T)=\Delta_0(T)\frac{k_z}{k_c}\cos(3\varphi)$	$\frac{k_c\beta}{\Delta_0(T)}\{0.656+\ln[\beta\Delta_0(T)]-\frac{15}{16[\beta\Delta_0(T)]^2}+\cdots\}$
Γ_4^+	$\Delta(\varphi,k_z;T)=\Delta_0(T)\frac{k_z}{k_c}\sin(3\varphi)$	$\frac{k_c\beta}{\Delta_0(T)}\{0.656+\ln[\beta\Delta_0(T)]-\frac{15}{16[\beta\Delta_0(T)]^2}+\cdots\}$

TABLE III. Low-temperature variation of the pair density, Eq. (4.8).

Irreducible representation	Gap parametrization	$-[n_S(T)/n_{TOTAL}-1]/C_3$ [Eq. (4.8)] Low-T variation for $\beta\Delta_0(T)\gg 1$
Γ_1^+	$\Delta(T)=\Delta_0(T)$	$4\pi k_c e^{-\beta\Delta_0(T)}\left(\sqrt{\beta\Delta_0(T)}+\frac{3}{8\sqrt{\beta\Delta_0(T)}}\right)$
Γ_1^+	$\Delta(k_z;T)=\Delta_0(T)k_z^2/k_c^2$	$2\pi k_c/\sqrt{\beta\Delta_0(T)}$
Γ_2^+	$\Delta(\varphi,T)=\Delta_0(T)\sin(6\varphi)$	$\frac{2\sqrt{\pi}k_c}{\beta\Delta_0(T)}\{2+\frac{15}{4[\beta\Delta_0(T)]^2}+\cdots\}$
Γ_3^+	$\Delta(\varphi,k_z;T)=\Delta_0(T)\frac{k_z}{k_c}\cos(3\varphi)$	$\frac{4\sqrt{\pi}k_c}{\beta\Delta_0(T)}\{0.656+\ln[\beta\Delta_0(T)]-\frac{15}{16[\beta\Delta_0(T)]^2}+\cdots\}$
Γ_4^+	$\Delta(\varphi,k_z;T)=\Delta_0(T)\frac{k_z}{k_c}\sin(3\varphi)$	$\frac{4\sqrt{\pi}k_c}{\beta\Delta_0(T)}\{0.656+\ln[\beta\Delta_0(T)]-\frac{15}{16[\beta\Delta_0(T)]^2}+\cdots\}$

$$\frac{n_s(T)}{n_{TOTAL}}=\left(\frac{\lambda(T=0)}{\lambda_0(T)}\right)^2 = 1-\frac{\beta\hbar^2}{12\pi^2 m n_{TOTAL}}\int_0^\infty dk k^4\,\mathrm{sech}^2\left(\frac{\beta}{2}\sqrt{\Delta_0^2+\xi(k)^2}\right). \tag{4.5}$$

Noting the functional form of the Fermi distribution and its derivative

$$f_{FERMI}(\beta,E)=\frac{1}{1+e^{\beta E}},\quad \frac{\partial f_{FERMI}(\beta,E)}{\partial E}=-\frac{\beta}{4}\mathrm{sech}^2\left(\frac{\beta E}{2}\right), \tag{4.6}$$

expression (4.5) yields precisely the textbook result.[33] In particular, inserting the expression applicable for parabolic band structure $n_{TOTAL}=\frac{1}{3\pi^2}\left(\frac{2m\mu}{\hbar^2}\right)^{3/2}$ (Ref. 33) and noting that $\mathrm{sech}^2 z\approx 4e^{-2z}$ for $z\gg 1$, yields the well-known low-temperature limit for an s-wave gap symmetry[34]

$$\frac{n_s(T)}{n_{TOTAL}}=1-[2\pi\Delta_0(T)\beta]^{1/2}e^{-\Delta_0(T)\beta}. \tag{4.7}$$

Note that the exponent in Eq. (4.7) is half of that in the corresponding IMD expression, Eq. (3.16), since the penetration depth does not involve squaring the constitutive-relation kernel.

To evaluate the low-temperature limit of Eq. (4.4) for a general gap symmetry we follow steps and arguments corresponding to those in Sec. III, since the fastest varying factor in the integrand of Eq. (4.4) is the $\mathrm{sech}^2(z)$. For $z\gg 1$ it follows that $\mathrm{sech}^2 z\approx 4e^{-2z}$. Skipping all intermediate steps, the final result is

$$\frac{n_S(T)}{n_{TOTAL}}=\left[\frac{\lambda(T=0)}{\lambda(T)}\right]^2 = 1-C_3\beta^{1/2}\int_0^{2\pi}d\varphi\int_{-k_c}^{k_c}dk_z[\Delta(\varphi,k_z)^2]^{1/4}\times e^{-\beta\sqrt{\Delta(\varphi,k_z)^2}}, \tag{4.8}$$

where all the slowly varying factors in temperature are lumped into the constant C_3. The integral term in Eq. (4.8) is identical with that in Eq. (3.15) except for the power of β prefactor, i.e., 1/2 vs 5/2. Hence, the low-temperature limit of Eq. (4.8) is readily deduced from Table II by the appropriate adjustment of the β-prefactor power. The results in Table III show that except for an s-wave gap symmetry, the temperature dependence of the penetration depth follows a power law and a logarithmic dependence in T.

So far, we have considered the one-band case. Unlike the IMD case where the contribution of the s-wave-dominated gap vanishes exponentially at low temperatures and can be neglected, in the case of the penetration depth contributions of both gaps in MgB_2 must be considered because both remain finite. As mentioned above and discussed in Sec. VII, we approximate the two gaps as uncoupled, each with a different predominant symmetry. In this approximation, the *linear* constitutive relation between the current and vector potential takes the generalized form

$$\vec{j}_S=\gamma\vec{j}_S(\sigma)+(1-\gamma)\vec{j}_S(\pi)\underbrace{=}_{LINEAR}-\frac{c}{4\pi}\left(\frac{\gamma}{\lambda_{0\sigma}^2}+\frac{1-\gamma}{\lambda_{0\pi}^2}\right)\vec{A} = -\frac{c}{4\pi}\frac{1}{\lambda_0^2}\vec{A}, \tag{4.9}$$

where γ denotes the relative weight of the σ- and π-band contributions and $\lambda_{0\sigma}(T)$ and $\lambda_{0\pi}(T)$ are evaluated according to Eq. (4.8) with the appropriate gaps. As will be shown below, the exact value of γ is unimportant when considering $\lambda(T)$ at low temperatures. From Eq. (4.9), the measured penetration depth λ_0 is given by

$$\frac{1}{\lambda_0^2(T)}=\frac{\gamma}{\lambda_{0\sigma}^2(T)}+\frac{1-\gamma}{\lambda_{0\pi}^2(T)}. \tag{4.10}$$

As Eq. (4.8) indicates, at low temperatures a convenient construct is the penetration-depth deviation with respect to a chosen (low, nonzero) reference temperature. For a finite reference temperature T_0 the measured deviation is defined as

$$\delta_0(T;T_0)\equiv\frac{\lambda_0(T)}{\lambda_0(T_0)}-1. \tag{4.11}$$

On the other hand, the calculated quantity in Eq. (4.8) refers to single-gap deviations with $T_0=0$. The relation between these two kinds of deviations is obtained by inserting the penetration-depth deviation in Eq. (4.11) and the analogous deviations for the π and σ gaps into Eq. (4.10), and invoking

the linear transformation between the deviations with respect to a finite T_0 and with respect to $T_0=0$. To the lowest order in the latter deviations, simple manipulations yield

$$\delta_0(T;T_0) = a_\sigma[\delta_\sigma(T;T_0=0) - \delta_\sigma(T_0;T_0=0)] + a_\pi[\delta_\pi(T;T_0=0) - \delta_\pi(T_0;T_0=0)],$$

$$\delta_i(T;T_0=0) = \frac{\lambda_{0i}(T)}{\lambda_{0i}(T_0=0)} - 1, \quad i=\sigma \text{ or } \pi. \quad (4.12)$$

In Eq. (4.12) the penetration-depth deviations on the right-hand side are calculated from Eq. (4.8) for the chosen T_0 and the pertaining gap symmetries. The measured quantity is the left-hand side, and both sides of the equation are related in terms of two fitting parameters a_σ and a_π. The explicit expressions of a_σ, a_π, and the value of the γ parameter, $\gamma \simeq 0.5$,[18] are not needed.

The dimensionless deviations calculated from Eq. (4.8), $[\lambda_{0i}(0)/\lambda_{0i}(T)]^2 = 1 - D_i$, are typically very small. Hence, in the context of Eq. (4.12) they are related to the penetration-depth deviations by

$$\delta_i(T;T_0=0) = \frac{\lambda_{0i}(T)}{\lambda_{0i}(0)} - 1 = \frac{1}{\sqrt{1-D_i}} - 1 \approx \frac{D_i}{2}, \quad \text{for } D_i \ll 1, \ i=\sigma,\pi. \quad (4.13)$$

V. COMPARISON OF THEORY AND MEASUREMENTS

The analysis in Secs. III and IV provides a framework for comparison with our measurements. As argued below, the clean-limit expressions in Secs. III and IV apply since there are strong grounds for assuming that no extrinsic effects mask the intrinsic low-temperature variation in our films.

A. IMD measurements

In Fig. 5(a) the low-temperature portion of the MgB_2 data of Fig. 1 is redrawn and compared with the four possible low-temperature variations listed in Table II. The comparison clearly indicates that the best fit to the available data is a gap with the $\ell=6$ symmetry (Γ_2^+), i.e.,

$$\Delta(\phi,T) = \Delta_0(T)\sin(6\phi) \Rightarrow P_{\mathrm{IMD}}(T) \propto T^{-2}. \quad (5.1)$$

Figure 5(b) is another presentation of the temperature variation of the IMD for several samples over the entire temperature range in comparison with the predicted $\ell=6$ gap symmetry $P_{\mathrm{IMD}}(T) \propto T^{-2}$ of Eq. (5.1). Note the good comparison. In the next section, we further discuss this result.

B. Penetration depth measurements

The proposed symmetry in Eq. (5.1) has ramifications on the low-temperature variation in penetration depth, see Eq. (4.8) and Table III. In particular, for the symmetry of Eq. (5.1), Table III (Γ_2^+) yields

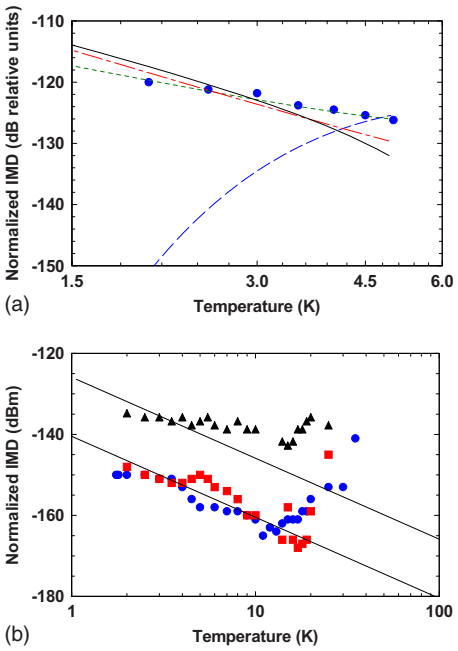

FIG. 5. (Color online) (a) Comparison of theory and experiment for several candidate symmetries. The points are the measured values for one of the 150-nm-thick films shown in Figs. 1 and 3. Long-dashed line, s wave or the first line of Table I (Γ_1^+); long-short-long-dashed line, the second line of Table I (Γ_1^+); short dashed line, third line of Table I (Γ_2^+); and solid line in black: fourth line of Table I (Γ_3^+). The Γ_2^+ curve yields the best fit to the data. (b) Comparison of the measured IMD with the $1/T^2$ prediction of the theory for the low-power, low-temperature asymptote of the IMD. The points are the same data as shown in Fig. 3 where ● is MgB_2 on LAO and ■ is MgB_2 on sapphire each at −5 dB m circulating power and ▲ is MgB_2 on sapphire at 0 dBm circulating power. The film thickness is 500 nm. The solid lines are simply $1/T^2$ behavior, which shows as a straight line on the double logarithmic plot.

$$\delta_\pi(T;T_0=0) = \frac{\lambda_\pi(T)}{\lambda_\pi(0)} - 1 = C_4\left\{2\left(\frac{1}{\beta(T)\Delta_0(T)}\right) + \frac{15}{4}\left(\frac{1}{\beta(T)\Delta_0(T)}\right)^3\right\}, \quad (5.2)$$

where C_4 is a temperature-independent constant, see the Appendix.

In Fig. 6 we plot the two-parameter fitting formula, Eq. (4.12), for two representative cases: (a) where we assume an s-wave gap symmetry for both gaps (the first Γ_1^+ presentation in Table III); (b) where the π gap has the proposed $\ell=6$ as the dominant symmetry [Eq. (5.2)] while the σ gap is predominantly s wave. The temperature dependencies $\Delta_0(T)$ are taken from Ref. 14. As Fig. 6 shows, cases (a) and (b) follow the data closely throughout the considered temperature domain with slightly different curvatures. Hence, the penetration depth data in Fig. 6 is *consistent* with the proposed $\ell=6$ π-gap symmetry of Eqs. (1.3) and (5.1). We note that a single s-wave gap with either the π or σ magnitude yields a poor fit.

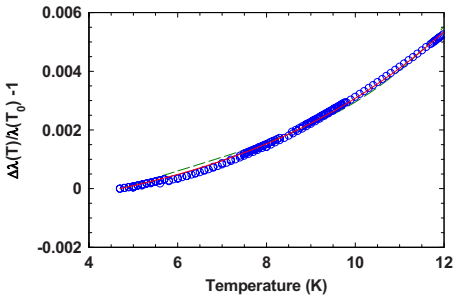

FIG. 6. (Color online) Comparison of the measured penetration depth deviation, $\lambda_0(T)/\lambda_0(T_0)-1$, Eq. (4.11), with the computed values for two different candidate symmetries. The open blue circles are the data for MgB_2 on sapphire at low power. The solid red line is the computed curve, Eq. (4.12), for the $\ell=6$ symmetry of the π gap and s-wave symmetry of the σ gap. The best fit yields approximately equal weights of the two gaps. The dashed green line is the computed curve, Eq. (4.12), for two s-wave gaps with approximately equal weights of the two gaps. Both fits compare with the data approximately equally well.

VI. POSSIBLE EXTRINSIC EFFECTS ON IMD

Thus far, we have presented the evidence that the low-temperature upturn in IMD and penetration-depth temperature dependence reflect the existence of nodal lines, specifically, the symmetry with six nodal lines, Eq. (1.3), most likely in the π-band energy gap. In the following, we examine the question of whether the observed upturn in the low-temperature IMD could result from extrinsic causes rather than the symmetry of the gap. We examine two of the most important extrinsic sources of nonlinearity, weak links, and two-level systems, and argue that neither of these can explain our experimental results.

A. Weak links

Defects and grain boundaries can be origins of weak links, and weak-link effects attributed to grain boundaries have been observed in MgB_2.[35] Weak links behave as Josephson junctions with critical currents that are smaller than the macroscopic value of the critical current. The existence and behavior of weak links are well documented and are known to provide sources of RF nonlinearities, such as IMD.[36–38] The IMD generated in a weak link is related to the weak-link critical current I_c. The smaller the I_c the larger the IMD.[38] Thus, the temperature dependence of the IMD generated by a weak link is related to that of the critical current $I_c(T)$, which is given by the Ambegaokar-Baratoff model[39]

$$I_c(T) = \frac{I_c(0)}{\sqrt{\left(1-\frac{T}{T_c}\right)}}. \tag{6.1}$$

Therefore, since the weak-link IMD is inversely related to I_c, Eq. (6.1) implies that it increases monotonically as the temperature increases and it is relatively constant at temperatures $T<T_c/2$. This has been demonstrated experimentally in Ref. 5, where the IMD of YBCO films on sapphire was found to be monotonic in temperature. Thus, weak links as the origin of the increase in IMD at low temperatures can be ruled out.

B. Two-level systems

Two-level systems (TLS) are saturable absorbers, which have been typically observed at low temperature in glasses.[40] TLS have also been observed in single-crystal MgO (Ref. 41) and β alumina[42] at temperatures comparable to 5 K. At low temperatures and low-power levels where the population difference between the two levels is maintained, the TLS absorb energy. At higher temperatures, or when the power is high enough to populate both levels equally, the TLS become inactive as absorbers because the populations of the upper and lower levels are equalized. Thus, TLS in a stripline resonator lead to anomalous resonator Q values as a function of power: the Q value increases as the circulating power in the resonator increases until saturation of the TLS occurs after which the Q vs power is constant. The opposite is observed in a superconductor, where, above a certain level, the Q decreases with increasing power. The saturation effects of the TLS are obviously nonlinear and produce IMD. In addition, since the TLS become active only at low temperatures, one would expect an increase in IMD at low temperatures as the TLS become active.

The unambiguous signature of TLS is the anomalous power dependence of the resonator Q and an anomalous temperature dependence of the low-power Q, showing a decrease in Q as the temperature is decreased.[41] In our measurements of MgB_2 these signatures of TLS are completely absent. None of the MgB_2 resonators show anomalous power or temperature dependence of the Q. In addition, the similar behavior of the IMD on sapphire and lanthanum aluminate substrates constitutes another reason for the exclusion of TLS as the explanation of the IMD vs T. TLS are associated with the substrate or the interface,[43] and therefore the similar behavior on different substrates indicates that TLS are an improbable explanation.

VII. RELATION OF OUR FINDINGS TO EXISTING LITERATURE

It is often stated that MgB_2 is a conventional s-wave superconductor.[12] While some data support this, the literature also contains numerous examples of measurements incompatible with s-wave gap symmetry. Here we consider whether the proposed symmetry, Eqs. (1.3) and (5.1), is consistent with the literature. As we shall show, some of the data are consistent with our symmetry proposition. Specifically, we consider data on specific heat, NMR, the penetration depth, and tunneling.

The electronic specific heat C_{es} played an important role in identifying the two-gap structure of MgB_2.[12,13] Its expression is[44,45]

$$C_{es} = \frac{V}{(2\pi)^3} 2\beta k_B \int d\vec{k}\left(-\frac{\partial f(E)}{\partial E}\right)\left(E^2 - T\Delta\frac{d\Delta}{dT}\right), \tag{7.1}$$

where V denotes the sample volume and the quasiparticle Fermi distribution function, Eq. (4.6), is

$$f = \frac{1}{e^{\beta E}+1}, \quad E = \sqrt{\xi^2(\vec{k})+\Delta^2}, \quad \Delta = \Delta(\vec{k},T). \quad (7.2)$$

At low temperatures, the $T\Delta(d\Delta/dT)$ term in Eq. (7.1) is negligible. Also, as argued in Secs. III and IV, the exponential factor in the quasiparticle Fermi distribution dominates, hence $\partial f(E)/\partial E \approx -\beta e^{-\beta E}$. These steps yield for the low-temperature specific heat

$$\begin{aligned} C_{es}(T) &\approx C_6\beta^2 \int d\xi \int_0^{2\pi} d\phi [\xi^2+\Delta^2(\phi)] e^{-\beta\sqrt{\xi^2+\Delta^2(\phi)}} \\ &\approx C_6\beta^2 \int d\xi \int_0^{2\pi} d\phi \Delta^2(\phi) e^{-\beta\sqrt{\xi^2+\Delta^2(\phi)}} \\ &= C_7\beta^{3/2} \int_0^{2\pi} d\phi \Delta^2(\phi) [\Delta^2(\phi)]^{1/4} e^{-\beta\sqrt{\Delta^2(\phi)}} \\ &\underset{\beta\to\infty}{\rightrightarrows} \beta^{3/2}\left(\frac{15\sqrt{\pi}}{2\beta^{7/2}}\right) \propto T^2, \end{aligned} \quad (7.3)$$

where we have assumed a gap with the $\ell=6$ symmetry. The temperature-independent constants C_6 and C_7 lump together all factors irrelevant in the present context, in analogy to the steps that led to Eq. (3.15). The exact ξ integration follows Eq. (3.14) while the exact ϕ integration for the $\ell=6$ gap symmetry, Eqs. (1.3) and (5.1), yields a complicated expression containing hypergeometric functions. In Eq. (7.3) only the $\beta\to\infty$ limit of that expression is quoted. Note that the low-T dependence of the specific heat in Eq. (7.3) applies also for a gap with a d-wave symmetry (not shown here). By comparison, the specific heat of an s-wave gap has the characteristic exponential temperature dependence, $e^{-\beta\Delta_0}$.

As Eq. (7.3) indicates, the $\ell=6$ nodal gap symmetry predicts that $C_{es}(T)/T \propto T$ at low temperatures. The low-temperature specific-heat measurements from four groups are consistent with this linear temperature variation in the temperature range of $2 \le T \le 10$ K, where presumably the π-gap contribution dominates.[46–50] In one paper the linear temperature dependence of $C_{es}(T)/T$ is explicitly interpreted to imply nodal lines in the gap.[49] The data for $T \le 2$ K vary among these groups, most likely reflecting experimental limitations. We note also that first-principles calculations based on a presumed s-wave π-gap symmetry[14,51] do not agree well with the data in the $2 \le T \le 10$ K temperature domain. Hence, we interpret these specific-heat measurements and calculations to be consistent with nodal lines.

Related to the low-temperature specific heat at zero magnetic field is the low-field variation, at low temperature, of the Sommerfeld constant γ, defined as $C_{es}(H,T)/T = \gamma(H)$. For an s-wave superconductor a linear-field dependence $\gamma(H) \propto H$ is expected,[52,53] while for a nodal gap, $\gamma(H) \propto H^{1/2}$.[54,55] The data from several groups vary in the details,[46,47,56–58] but in all cases at low fields the data follow $\gamma(H) \propto H^n$ with $0 < n < 1$. Clear low-temperature low-field dependence $\gamma(H) \propto H^{1/2}$ is reported in recent single-crystal experiments[56–58] which is in direct support of the proposed π-gap symmetry of Eq. (1.3). The other reported field dependencies of the $\gamma(H)$ in polycrystalline samples[46,47] may be related to the microstructure. Thus, in no case to our knowledge does the Sommerfeld-constant data preclude the nodal-gap symmetry proposed here.

A second class of experiments employing a bulk probe that reflect on the gap symmetry are NMR studies, where $[T_{1S}(T)]^{-1}$, the inverse of the nuclear spin-lattice relaxation rate, is measured as function of temperature. The gap symmetry is reflected in two features of $[T_{1S}(T)]^{-1}$, the Hebel-Schlichter peak (also, referred to as the coherence peak) at temperatures just under T_c (Refs. 59 and 60) and the characteristic low-temperature variation. For a nodal gap, such as the d-wave gap symmetry in YBCO, the Hebel-Schlichter peak is absent[61,62] while for an s-wave gap this peak is prominent and provided one of the first successes of the BCS theory.[60] At low temperatures $[T_{1S}(T)]^{-1} \propto T^3$ for a nodal gap[19] while for a s-wave gap, $[T_{1S}(T)]^{-1}$ decays exponentially. Most experiments measured the ^{11}B NMR response. The experiment in Ref. 63 reports a small Hebel-Schlichter peak, followed by an exponential drop with decreasing temperature. This exponential drop supports an s-wave gap symmetry for the σ gap which dominates the temperature range near T_c. The data stops at $T=12$ K where it is expected that the low-temperature variation will start to dominate. A similar small Hebel-Schlichter peak was observed by another group[64] while other groups do not observe it at all.[65–68] The issue of the Hebel-Schlichter peak in MgB_2 is to our knowledge still open.[62] As for the low-field low-temperature variation in $[T_{1S}(T)]^{-1}$, the data in Ref. 64 (down to $T=5$ K) show a markedly slower decrease with temperature than an exponential decay. Similarly, in Ref. 65 the single experimental point shown for $T=2$ K clearly deviates from the exponential decay observed at higher temperatures. In summary, the low-temperature NMR data reviewed here is inconsistent with an s-wave gap symmetry, whereas the measurements of the Hebel-Schlichter peak are inconsistent among the various groups, where some of the data indicate the existence of a nodal gap.

Consider now the experimental situation regarding the low-temperature penetration depth. As demonstrated in Sec. V, our measured low-temperature penetration-depth data compare well with the prediction of the presumed nodal gap of Eq. (1.3). However, as demonstrated in Fig. 6 over a limited low-temperature range our data are hardly distinguishable from a model with both π and σ gaps having pure s-wave symmetries as suggested by one set of data.[69] From experience with YBCO, however, it seems that it is necessary to reach temperatures well below $0.05T_c$ to differentiate between different symmetries by methods of microwave response.[70] Other data, derived from muon spin rotation[71] and optical conductivity,[72] yield the penetration-depth $\propto T^2$ while an ac susceptibility experiment fits the penetration-depth data with a temperature dependence $T^{2.7}$.[73] These works are clearly inconsistent with the exponential falloff expected for a s-wave gap, Eq. (4.7). Thus, to our knowledge the penetration-depth data as a probe of the gap symmetry has not yet reached a consensus.

Tunneling spectroscopy has the capacity to discern the gap symmetry, but it has the disadvantage of sensitivity to surface quality. The measured quantity is the low-

temperature conductance $G(V)=dI/dV$ where I and V denote the current and voltages across a tip. This observable measures the density of states as function of excitation energy. For a gap with nodal lines in the $\widehat{ab}$ plane, the conductance signature is a V-shaped minimum for tunneling in the $\hat{c}$ direction, centered at $V=0$.[74] On the other hand, for an s-wave gap the conductance vanishes over the voltage range $-\Delta \leq eV \leq \Delta$, indicating zero density of states below the gap. As with the probes mentioned above, not all data are consistent with each other. In one experiment[75] at $T=0.32$ K with a single crystal, a $G=0$ flat voltage minimum was observed and interpreted to imply an s-wave superconductor. However, the extension of that flat minimum is ≈ 2 meV, about half of the expected extension $2\Delta_\pi \approx 4$ meV.[12] Another study, with a sputtered MgB_2 film at $T=1.5$ K, finds a flat conductance minimum of the correct extension; however, $G \neq 0$ at the conductance minimum as expected for a s-wave gap.[76] Other groups find a V-shaped conductance minimum, which is consistent with a nodal gap, Eq. (1.3).[77,78]

The above data survey indicates that there is no low-temperature experimental consensus regarding the π-gap symmetry. While some experiments suggest s-wave symmetry others support the notion of a gap with nodal lines. The IMD and penetration-depth measurements reported here are consistent with the existence of a gap with symmetry that entails six nodal lines. The advantage of the IMD probe invoked in this work is its clear nodal gap signature, as articulated in Eqs. (1.1) and (1.2), and the relative simplicity of the interpretation.[3,5]

VIII. SUMMARY AND CONCLUSIONS

Our analysis assumes that the σ and π gaps are effectively decoupled. However, since MgB_2 exhibits a single critical temperature, some coupling between them must exist[16] and hence both the σ and π gaps have a small admixture of the symmetry of the other gap: s-wave symmetry for the π gap and $\ell=6$ symmetry for the σ gap. This admixture of a minority component to the order parameter does not affect the low-temperature T^{-2} divergence of the IMD since the contribution of the nodal lines at low temperatures dominates. In support of this conclusion note a similar situation for YBCO, believed to have a d-wave gap symmetry. Evidence has recently been presented that YBCO entails a small amount of s-wave coupled into the predominant d-wave symmetry,[10] yet in high-quality YBCO films the low-temperature T^{-2} divergence is a prominent feature of the IMD.[3–7] Furthermore, a recent calculation of the d- and s-wave gap coupling in YBCO (Ref. 11) reveals a temperature dependence of the gap reminiscent of that measured for MgB_2.[13]

Our low-temperature IMD-power measurements on high-quality MgB_2 thin films are inconsistent with pure s-wave symmetry of the order parameter. The data provide a strong indication that at least one of the two energy gaps contains a component that exhibits a symmetry with nodal lines, specifically the $\ell=6$ symmetry, $\Delta(\phi,T)=\Delta_0(T)\sin(6\phi)$, with six nodal lines. This is the maximum number of nodal lines for the hexagonal crystal symmetry, in analogy to the d-wave gap symmetry in YBCO, which contains the maximum number of nodal lines for the tetragonal crystal symmetry. Both IMD and penetration-depth data are consistent with the assertion that the dominant symmetry of the π gap is the $\ell=6$ symmetry.

A review of the existing literature pertinent to gap symmetry reveals a lack of consensus, where experiments such as muon spin-rotation, some specific-heat experiments, and some data on the low-field variation in the Sommerfeld constant are in support the $\ell=6$ symmetry. This situation calls for additional experiments sensitive to the gap symmetry to resolve the issue. Following the developments that established the d-wave gap symmetry in YBCO,[79] we can suggest examining the existence or absence of a zero-bias anomaly for tunneling in specific $\widehat{ab}$ plane directions[74] or establishing a fractional flux vortex in a tricrystal experiment.[80]

ACKNOWLEDGMENTS

This work was supported by the Department of the Navy. Y.D.A. thanks support from the ILIR foundation of NSWCCD and insightful exchanges with A. S. Alexandrov.

APPENDIX: NONLINEAR KERNEL $K^{(2)}$ LOW-TEMPERATURE VARIATION

The first nontrivial application of Eq. (3.15) is for the Γ_1^+ gap that entails one nodal plane. A simple change in variables yields

$$K^{(2)}(q_z=0;\pi;T) \propto \beta^{5/2}\sqrt{\Delta_0(T)}\int_0^1 dx x e^{-\beta\Delta_0(T)x^2} = \frac{\beta^{3/2}}{\sqrt{\Delta_0(T)}}(1-e^{-\beta\Delta_0(T)}) \approx \frac{\beta^{3/2}}{\sqrt{\Delta_0(T)}} \tag{A1}$$

The next case is the Γ_2^+ gap, which entails six nodal lines, the maximum possible for the hexagonal crystal structure. In this case Eq. (3.15) has an analytic expression

$$\begin{aligned} K^{(2)}(q_z=0;\pi;T) &\propto \beta^{5/2}\sqrt{\Delta_0(T)}\int_0^{2\pi} dx[\sin^2(\ell x)]^{1/4} e^{-\beta\Delta_0(T)\sqrt{\sin^2(\ell x)}} \\ &= [\beta^{5/2}\sqrt{\Delta_0(T)}][\sqrt{2}\pi^{3/2}\sqrt{\beta\Delta_0(T)}] \\ &\times\left\{ I_{-3/4}\left[\frac{\beta\Delta_0(T)}{2}\right] I_{1/4}\left[\frac{\beta\Delta_0(T)}{2}\right] \right. \\ &\left. - I_{-1/4}\left[\frac{\beta\Delta_0(T)}{2}\right] I_{3/4}\left[\frac{\beta\Delta_0(T)}{2}\right] \right\} \end{aligned} \tag{A2}$$

for $\ell=2,4,6$ and where the symbol I denotes the modified Bessel functions of the first kind. The integral in Eq. (A2) remains unchanged if we replace in it the function sin with cos. With a focus on the low-temperature variation, consider the limit of Eq. (A2) for $\beta\Delta_0(T) \gg 1$. The leading terms in this limit are

$$[\sqrt{2}\pi^{3/2}\sqrt{\beta\Delta_0(T)}]\left\{I_{-3/4}\left[\frac{\beta\Delta_0(T)}{2}\right]I_{1/4}\left[\frac{\beta\Delta_0(T)}{2}\right] - I_{-1/4}\left[\frac{\beta\Delta_0(T)}{2}\right]I_{3/4}\left[\frac{\beta\Delta_0(T)}{2}\right]\right\} = \frac{\sqrt{\pi}}{[\beta\Delta_0(T)]^{3/2}}\left\{2+\frac{15}{4[\beta\Delta_0(T)]^2}+\cdots\right\} \quad \text{for} \quad \beta\Delta_0(T)\gg 1. \tag{A3}$$

Combining Eqs. (A2) and (A3) and taking the low-temperature limit yields for this case

$$K^{(2)}(q_z=0;\pi;T)\propto\frac{\beta}{\Delta_0(T)}\left\{2+\frac{15}{4[\beta\Delta_0(T)]^2}+\cdots\right\} \quad \text{for} \quad \beta\Delta_0(T)\gg 1. \tag{A4}$$

The other two gap symmetries in Table I, i.e., Γ_3^+ and Γ_4^+ have nodal lines *and* a nodal plane. They yield *exactly* the same low-temperature variation when inserted in Eq. (3.10). The exact double integration in Eq. (3.15) is available in closed form; however, its rather complex from is not quoted here. Instead, we quote here only the $\beta\Delta_0(T)\gg 1$ limit of that expression, i.e.,

$$K^{(2)}(q_z=0;\pi;T)\propto\beta^{5/2}\sqrt{\Delta_0(T)}\times\left\{4\frac{-2+\gamma+\ln(8)+\ln[\beta\Delta_0(T)]}{[\beta\Delta_0(T)]^{3/2}}-\frac{15}{4[\beta\Delta_0(T)]^{7/2}}+\cdots\right\} = \frac{4\beta}{\Delta_0(T)}\left\{0.656+\ln[\beta\Delta_0(T)]-\frac{15}{16[\beta\Delta_0(T)]^2}+\cdots\right\} \quad \text{for} \quad \beta\Delta_0(T)\gg 1. \tag{A5}$$

We have checked numerically that Eq. (A5) provides an excellent approximation for $\beta\Delta_0(T)\geq 2$.

For the low-temperature $[\beta\Delta_0(T)\gg 1]$ specific-heat calculation, Eq. (7.3), the following integral exists in a closed, yet rather complex form. Its low-temperature limit is

$$\int_0^{2\pi} dx\,\sin^2(\ell x)[\sin^2(\ell x)]^{1/4}e^{-\beta\Delta_0(T)\sqrt{\sin^2(\ell x)}} = \frac{15\sqrt{\pi}}{2[\beta\Delta_0(T)]^{(7/2)}}+\cdots \quad \text{for} \quad \beta\Delta_0(T)\gg 1. \tag{A6}$$

[1] S. K. Yip and J. A. Sauls, Phys. Rev. Lett. **69**, 2264 (1992); D. Xu, S. K. Yip, and J. A. Sauls, Phys. Rev. B **51**, 16233 (1995).
[2] T. Dahm and D. J. Scalapino, J. Appl. Phys. **81**, 2002 (1997); Phys. Rev. B **60**, 13125 (1999).
[3] D. Agassi and D. E. Oates, Phys. Rev. B **72**, 014538 (2005); **74**, 024517 (2006).
[4] D. E. Oates, S.-H. Park, and G. Koren, Phys. Rev. Lett. **93**, 197001 (2004).
[5] D. E. Oates, S.-H. Park, D. Agassi, G. Koren, and K. Irgmaier, IEEE Trans. Appl. Supercond. **15**, 3589 (2005).
[6] D. E. Oates, S. H. Park, D. Agassi, and G. Koren, Supercond. Sci. Technol. **17**, S290 (2004).
[7] D. E. Oates, J. Supercond. Novel Magn. **20**, 3 (2007).
[8] K. T. Leong, J. C. Booth, and S. A. Schima, IEEE Trans. Appl. Supercond. **15**, 3608 (2005).
[9] G. Cifariello, M. Aurino, E. Di Gennaro, G. Lamura, P. Orgiani, J.-C. Villégier, X. X. Xi, and A. Andreone, J. Phys.: Conf. Ser. **43**, 702 (2006).
[10] R. Khasanov, S. Strässle, D. Di Castro, T. Masui, S. Miyasaka, S. Tajima, A. Bussmann-Holder, and H. Keller, Phys. Rev. Lett. **99**, 237601 (2007).
[11] A. Bussmann-Holder, R. Khasanov, A. Shengelaya, A. Maisuradze, F. La Mattina, H. Keller, and K. A. Müller, EPL **77**, 27002 (2007).
[12] X. X. Xi, Rep. Prog. Phys. **71**, 116501 (2008).
[13] P. C. Canfield and G. W. Crabtree, Phys. Today **56** (3), 34 (2003).
[14] H. J. Choi, D. Roundy, H. Sun, M. L. Cohen, and S. G. Louie, Nature (London) **418**, 758 (2002).
[15] J. Kortus, I. I. Mazin, K. B. Belashchenko, V. Antropov, and L. L. Boyer, Phys. Rev. Lett. **86**, 4656 (2001).
[16] H. Suhl, B. T. Matthias, and L. R. Walker, Phys. Rev. Lett. **3**, 552 (1959).
[17] V. Z. Kresin, J. Low Temp. Phys. **11**, 519 (1973).
[18] I. I. Mazin, O. K. Andersen, O. Jepsen, O. V. Dolgov, J. Kortus, A. A. Golubov, A. B. Kuz'menko, and D. van der Marel, Phys. Rev. Lett. **89**, 107002 (2002).
[19] M. Sigrist and K. Ueda, Rev. Mod. Phys. **63**, 239 (1991).
[20] B. H. Moeckly, K. E. Kihlstrom, A. Findikoglu, and D. Oates, IEEE Trans. Appl. Supercond. **15**, 3308 (2005).
[21] B. H. Moeckly and W. S. Ruby, Supercond. Sci. Technol. **19**, L21 (2006).
[22] L. Gu, B. H. Moeckly, and D. J. Smith, J. Cryst. Growth **280**, 602 (2005).
[23] D. M. Sheen, S. M. Ali, D. E. Oates, R. S. Withers, and J. A. Kong, IEEE Trans. Appl. Supercond. **1**, 108 (1991).
[24] W. S. Chow, Phys. Rev. **176**, 525 (1968).
[25] A. Bussmann-Holder, R. Mincas, and A. R. Bishop, Eur. Phys. J. B **37**, 345 (2003).
[26] L. P. Gor'kov and E. Rashba, Phys. Rev. Lett. **87**, 037004 (2001).
[27] I. S. Gradstein and I. M. Ryzhik, *Tables of Integrals, Series, and Products* (Academic, New York, 1965), p. 959, Eq. (9).
[28] M. Abramowitz and I. Stegun, *Handbook of Mathematical Functions* (U.S. GPO, Washington, D.C., 1964), p. 378.
[29] J. M. An and W. E. Pickett, Phys. Rev. Lett. **86**, 4366 (2001).
[30] Y. Kong, O. V. Doglov, O. Jepsen, and O. K. Andersen, Phys. Rev. B **64**, 020501 (2001).
[31] D. Agassi and D. E. Oates (unpublished).
[32] M. Tinkham, *Introduction to Superconductivity* (McGraw-Hill,

New York, 1975).
[33] A. F. Fetter and J. D. Walecka, *Quantum Theory of Many-Particle Systems* (McGraw-Hill, New York, 1971), p. 46.
[34] A. A. Abrikosov, *Fundamentals of the Theory of Metals* (North-Holland, Amsterdam, 1988), p. 364.
[35] A. A. Gallitto, G. Bonsignore, G. Giunchi, and M. J. Li Vigni, J. Supercond. Novel Magn. **20**, 13 (2007).
[36] T. L. Hylton and M. R. Beasley, Phys. Rev. B **39**, 9042 (1989).
[37] J. Halbritter, J. Supercond. **19**, 547 (2006).
[38] H. Xin, D. E. Oates, G. Dresselhaus, and M. S. Dresselhaus, Phys. Rev. B **65**, 214533 (2002).
[39] A. Barone and G. Paternò, *Physics and Applications of the Josephson Effect* (Wiley-Interscience, New York, 1982).
[40] W. A. Phillips, J. Low Temp. Phys. **7**, 351 (1972).
[41] M. A. Hein, D. E. Oates, P. J. Hirst, R. G. Humphreys, and A. V. Velichko, Appl. Phys. Lett. **80**, 1007 (2002).
[42] U. Strom, M. von Schickfus, and S. Hunklinger, Phys. Rev. Lett. **41**, 910 (1978).
[43] R. Barends, H. L. Hortensius, T. Zijlstra, J. J. A. Baselmans, S. J. C. Yates, J. R. Gao, and T. M. Klapwijk, Appl. Phys. Lett. **92**, 223502 (2008).
[44] M. Tinkham, *Introduction to Superconducitivity* (Ref. 32), p. 64.
[45] J. B. Ketterson and S. N. Song, *Superconductivity* (Cambridge University Press, Cambridge, U.K., 2003), p. 215.
[46] H. D. Yang, J.-Y. Lin, H. H. Li, F. H. Hsu, C. J. Liu, S.-C. Li, R.-C. Yu, and C.-Q. Jin, Phys. Rev. Lett. **87**, 167003 (2001).
[47] F. Bouquet, R. A. Fisher, N. E. Phillips, D. G. Hinks, and J. D. Jorgensen, Phys. Rev. Lett. **87**, 047001 (2001).
[48] Y. Wang, B. Revaz, A. Erb, and A. Junod, Phys. Rev. B **63**, 094508 (2001).
[49] Y. Wang, T. Plackowski, and A. Junod, Physica C **355**, 179 (2001).
[50] M. Putti, A. Affronte, C. Ferdeghini, C. Tarantini, and E. Lehman, Phys. Rev. Lett. **96**, 077003 (2006).
[51] A. Floris, G. Profeta, N. N. Lathiotakis, M. Lüders, M. A. L. Marques, C. Franchini, E. K. U. Gross, A. Continenza, and S. Massidda, Phys. Rev. Lett. **94**, 037004 (2005).
[52] A. L. Fetter and P. C. Hohenberg, in *Superconductivity*, edited by R. D. Parks (Dekker, New York, 1969), Vol. 2, p. 919.
[53] C. Caroli, P. G. deGennes, and J. Matricon, Phys. Lett. **9**, 307 (1964).
[54] G. E. Volovik, JEPT Lett. **58**, 469 (1993).
[55] I. Vekhter, P. J. Hirschfeld, J. P. Carbotte, and E. J. Nicol, Phys. Rev. B **59**, R9023 (1999); C. Kubert and P. J. Hirschfeld, Phys. Rev. Lett. **80**, 4963 (1998).
[56] T. Klein, L. Lyard, J. Marcus, Z. Holanova, and C. Marcenat, Phys. Rev. B **73**, 184513 (2006).
[57] Z. Pribulova, T. Klein, J. Marcus, C. Marcenat, F. Levy, M. S. Park, H. G. Lee, B. W. Kang, S. I. Lee, S. Tajima, and S. Lee, Phys. Rev. Lett. **98**, 137001 (2007); Z. Pribulova, T. Klein, J. Marcus, C. Marcenat, M. S. Park, H.-S. Lee, H.-G. Lee, and S.-I. Lee, Phys. Rev. B **76**, 180502(R) (2007).
[58] L. Lyard, T. Klein, J. Marcus, R. Brusetti, C. Marcenat, M. Konczykowski, V. Mosser, K. H. Kim, B. W. Kang, H. S. Lee, and S. I. Lee, Phys. Rev. B **70**, 180504 (R) (2004).
[59] J. B. Ketterson and S. N. Song, *Superconductivity* (Ref. 45), p. 248.
[60] M. Tinkham, *Introduction to Superconductivity* (Ref. 32), p. 84.
[61] M. Tinkham, *Introduction to Superconductivity* (Ref. 32), p. 382; N. Bulut and D. J. Scalapino, Phys. Rev. Lett. **68**, 706 (1992).
[62] K. V. Samokhin and B. Mitrovic, Phys. Rev. B **72**, 134511 (2005); B. Mitrovic and K. V. Samokhin, *ibid.* **74**, 144510 (2006).
[63] H. Kotegawa, K. Ishida, Y. Kitaoka, T. Muranaka, and J. Akimitsu, Phys. Rev. Lett. **87**, 127001 (2001); H. Kotegawa, K. Ishida, Y. Kitaoka, T. Muranaka, N. Nakagawa, H. Takagiwa, and J. Akimitsu, Phys. Rev. B **66**, 064516 (2002).
[64] M. Karayanni, G. Papavassiliou, M. Pissas, M. Fardis, K. Papagelis, K. Prassides, T. Takenobu, and Y. Iwasa, J. Supercond. **18**, 521 (2005).
[65] E. Pavarini, S. H. Baek, B. J. Suh, F. Borsa, S. L. Bud'ko, and P. C. Canfield, Supercond. Sci. Technol. **16**, 147 (2003).
[66] A. Garashnko, K. Mikhalev, S. Verkhoskii, T. Dyachkova, A. Tyutyunnik, and V. Zubkov, Appl. Magn. Reson. **21**, 157 (2001).
[67] S. H. Baek, B. J. Suh, E. Pavarini, F. Borsa, R. G. Barnes, S. L. Bud'ko, and P. C. Canfield, Phys. Rev. B **66**, 104510 (2002).
[68] J. K. Jung, S. H. Baek, F. Borsa, S. L. Bud'ko, G. Lapertot, and P. C. Canfield, Phys. Rev. B **64**, 012514 (2001).
[69] F. Manzano, A. Carrington, N. E. Hussey, S. Lee, A. Yamamoto, and S. Tajima, Phys. Rev. Lett. **88**, 047002 (2002).
[70] W. N. Hardy, D. A. Bonn, D. C. Morgan, R. Liang, and K. Zhang, Phys. Rev. Lett. **70**, 3999 (1993); P. J. Hirschfeld and N. Goldenfeld, Phys. Rev. B **48**, 4219 (1993).
[71] C. Panagopoulos, B. D. Rainford, T. Xiang, C. A. Scott, M. Kambara, and I. H. Inoue, Phys. Rev. B **64**, 094514 (2001).
[72] A. V. Pronin, A. Pimenov, A. Loidl, and S. I. Krasnosvobotsev, Phys. Rev. Lett. **87**, 097003 (2001).
[73] X. Y. Chen, Y. Y. Xue, R. L. Ming, and C. W. Chu, Phys. Rev. B **64**, 172501 (2001).
[74] H. Castro, G. Leibovitch, R. Beck, A. Kohen, Y. Dagan, and G. Deutscher, Microelectron. J. **39**, 1296 (2008); R. Krupke and G. Deutscher, Phys. Rev. Lett. **83**, 4634 (1999).
[75] M. R. Eskildsen, M. Kugler, S. Tanaka, J. Jun, S. M. Kazakov, J. Karpinski, and Ø. Fischer, Phys. Rev. Lett. **89**, 187003 (2002).
[76] J. Geerk, R. Schneider, G. Linker, A. G. Zaitsev, R. Heid, K.-P. Bohnen, and H. v. Löhneysen, Phys. Rev. Lett. **94**, 227005 (2005).
[77] F. Giubileo, D. Roditchev, W. Sacks, R. Lamy, D. X. Thanh, and J. Klein, Phys. Rev. Lett. **87**, 177008 (2001).
[78] K. M. Iavarone, G. Karapetrov, A. E. Koshelev, W. K. Kwok, G. W. Crabtree, and D. G. Hinks, Phys. Rev. Lett. **89**, 187002 (2002).
[79] D. J. Scalapino, Phys. Rep. **250**, 329 (1995).
[80] C. C. Tsuei, J. R. Kirtley, C. C. Chi, Lock See Yu-Jahnes, A. Gupta, T. Shaw, J. Z. Sun, and M. B. Ketchen, Phys. Rev. Lett. **73**, 593 (1994).